Chemistry–A European Journal
Research Article
doi.org/10.1002/chem.202201295
Chemistry Europe
European Chemical Societies Publishing
www.chemeurj.org

VIP Synchrotron X-ray Electron Density Analysis of Chemical Bonding in the Graphitic Carbon Nitride Precursor Melamine

Emilie S. Vosegaard,[a] Maja K. Thomsen,[a] Lennard Krause,[a] Thomas B. E. Grønbech,[a] Aref Mamakhel,[a] Seiya Takahashi,[b] Eiji Nishibori,[b] and Bo B. Iversen*[a]

Abstract: Melamine is a precursor and building block for graphitic carbon nitride (g-CN) materials, a group of layered materials showing great promise for catalytic applications. The synthetic pathway to g-CN includes a polycondensation reaction of melamine by evaporation of ammonia. Melamine molecules in the crystal organize into wave-like planes with an interlayer distance of 3.3 Å similar to that of g-CN. Here we present an extensive investigation of the experimental electron density of melamine obtained from modelling of synchrotron radiation X-ray single-crystal diffraction data measured at 25 K with special focus on the molecular geometry and intermolecular interactions. Both intra- and interlayer structures are dominated by hydrogen bonding and π-interactions. Theoretical gas-phase optimizations of the experimental molecular geometry show that bond lengths and angles for atoms in the same chemical environment (C–N bonds in the ring, amine groups) differ significantly more for the experimental geometry than for the gas-phase-optimized geometries, indicating that intermolecular interactions in the crystal affects the molecular geometry. In the experimental crystal geometry, one amine group has significantly more sp^3-like character than the others, hinting at a possible formation mechanism of g-CN. Topological analysis and energy frameworks show that the nitrogen atom in this amine group participates in weak intralayer hydrogen bonding. We hypothesize that melamine condenses to g-CN within the layers and that the unique amine group plays a key role in the condensation process.

Introduction

Melamine (2,4,6-triamino-*s*-triazine) is a starting material for many compounds with industrial applications, for example, laminate products, adhesives and flame retardants.[1] In recent years, interest in melamine has increased as it is the precursor for graphitic carbon nitride (g-CN) materials,[2] a type of material showing promise in a variety of applications including metal-free heterogeneous electro- and photocatalysis for water splitting, CO_2 reduction and other conversion reactions as summarized in the review by Qi et al.[3] Using organic materials for catalysis has many advantages such as high abundance, low cost and easy preparation, as well as the ability to produce sustainable and lightweight products. The structure of g-CN has been proposed to consist of layers of extended graphite-like CN arrangements with a stoichiometry close to that of C_3N_4, but due to its amorphous character direct structure determination is difficult.[4]

General attempts to reason structures of g-CN have been made, but in most cases, only the stochiometry has been experimentally determined using, for example, elemental analysis. An idea of a structural motif has been comprised from Raman-, infrared spectroscopy, mass spectrometry, solid-state nuclear magnetic resonance (NMR) and especially comparison with spectra obtained from simulations of the structurally similar Si_3N_4 has given valuable insight.[5–7] Only very few g-CN-like structures have been studied by single-crystal or powder X-ray diffraction (SCXRD or PXRD).[8–10] PXRD shows only a single peak corresponding to a stacking distance of 3.3 Å[4,11] and based on ab initio calculations of solid-state NMR spectra Sehnert et al. found that the 2D layers form buckled wave planes due to lone pair repulsion between nitrogen atoms.[7]

Due to the structural and stoichiometric similarities between melamine and g-CN, the melamine molecule is regarded the smallest molecular unit to represent g-CN materials. Several studies report that the synthetic pathway to g-CN includes polycondensation of melamine with ammonia as the by-product.[4,8,12–13] The first step in the condensation of melamine

[a] E. S. Vosegaard, Dr. M. K. Thomsen, Dr. L. Krause, T. B. E. Grønbech, Dr. A. Mamakhel, Prof. Dr. B. B. Iversen
Department of Chemistry and iNANO
Aarhus University
Langelandsgade 140, 8000 Aarhus C (Denmark)
E-mail: bo@chem.au.dk

[b] S. Takahashi, Prof. Dr. E. Nishibori
Department of Physics
Faculty of Pure and Applied Sciences and
Tsukuba Research Center for Energy Materials Science (TREMS)
University of Tsukuba
Tsukuba, Ibaraki 305-8571 (Japan)

Supporting information for this article is available on the WWW under https://doi.org/10.1002/chem.202201295

is a dimerization to melam, as can be seen in Figure 1, followed by further condensation to either triazine or heptazine based g-CN. Consistent with the polycondensation reaction pathway, the g-CN structure shown in Figure 1, is an example of a proposed structure closely related to that of melamine with *s*-triazine rings connected through tertiary nitrogen bridges forming extended 2D layers.[12,14] Insight into the electronic properties of precursor materials such as melamine could be valuable for understanding the synthetic pathway to g-CN materials, and also form a basis for eventual structure and bonding clarification of g-CN.

This study presents a thorough investigation of the experimental electron density (ED) of melamine obtained at 25 K from synchrotron X-ray diffraction data with special focus on the molecular geometry and intermolecular interactions. Melamine crystalizes in the monoclinic space group $P2_1/n$ with a full molecule in the asymmetric unit, and four molecules in the unit cell. The crystal structure contains a comprehensive network of intermolecular interactions. On a shorter scale (unit cell size), the network seems three dimensional, but on a larger scale the molecules form wave-like planes with hydrogen bonds and π-interactions both in and between the layers. The structure of melamine on different length scales, as well as the naming convention, which will be used throughout this study can be seen in Figure 2. The distance between the layers is 3.3 Å, agreeing well with the layer distance in g-CN. The aromatic *s*-triazine ring and the attached amine-nitrogen atoms form an almost planar structure with the amine hydrogen atoms bent significantly out of the plane. The N–C–N angle in the ring is slightly larger (~125°) than the C–N–C angle (~115°) leaving more room for the nitrogen lone pair. In this study, analysis of the molecular geometry of melamine in the crystal is compared with theoretical gas phase calculations.

Here we analyze the experimental ED of melamine crystals in terms of chemical interactions. In particular, Bader topology, energy framework, electrostatic potential and noncovalent interaction (nci) calculations are used to study the chemical importance of the intermolecular interactions in the condensation of melamine. The first crystal structure of melamine was solved almost a century ago,[15] and since then several attempts to analyze intermolecular interactions through the ED have been made.[16–19] Here we provide an extensive analysis of the experimental ED based on highest quality synchrotron X-ray diffraction data at 25 K. The results derived from the experimental ED are in agreement with periodic theoretical calculations.

Results and Discussion

Molecular geometry

The melamine molecule forms two types of resonance structures as shown in Figure 3: one where the aromatic system in the ring persists and the amine groups are sp^3 hybridized (Figure 3 top), and another where one or more of the amine nitrogen atoms donate a lone pair and become sp^2 hybridized (Figure 3 bottom) to create a double bond, and thus become part of the conjugated system.

In the theoretical case where three equivalent groups are bonded to a central atom, the pure sp^2 hybridized orbital geometry would be a perfect plane with an angle of 120°

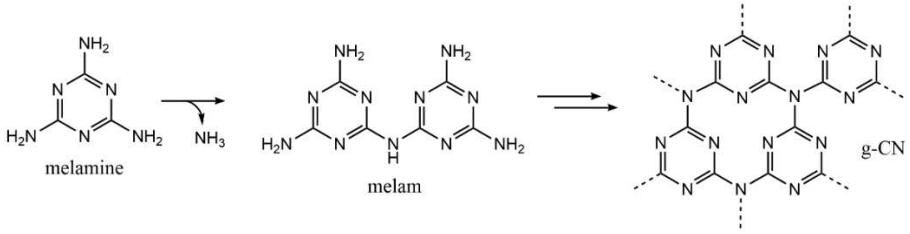

Figure 1. Polycondensation reactions of melamine through melam to a proposed structure of triazine based g-CN.

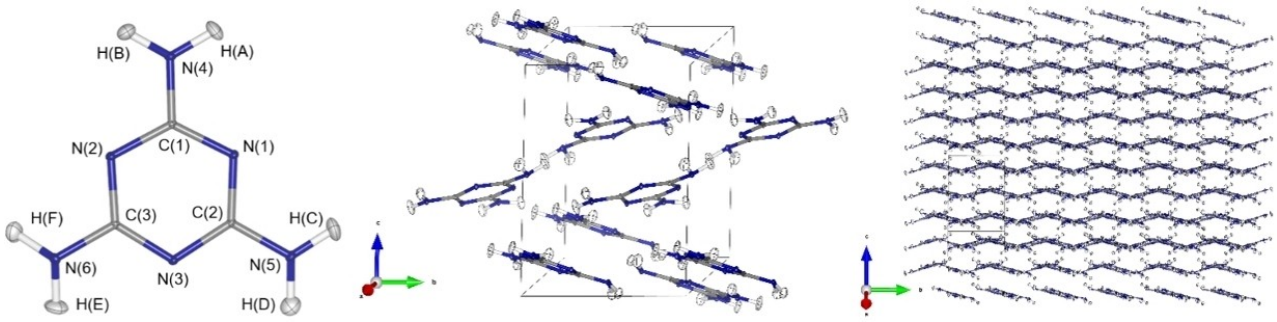

Figure 2. Schematics of the melamine molecule (asymmetric unit) with naming as it will be used throughout this study, the melamine unit cell and the wavy layers on larger scale. Atoms are shown as 50% probability ellipsoids.

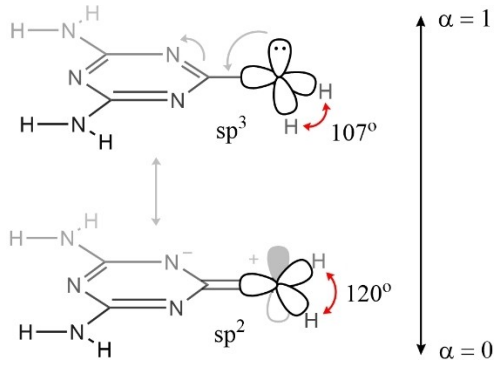

Figure 3. Resonance structures of melamine including visualized hybridized orbitals. α is the pyramidality of the resonance structures.

between each group. On the other hand, if the central nitrogen atom is sp^3 hybridized, but with one orbital occupied by a lone pair, the molecule would form a trigonal pyramidal geometry with an angle of 107°, like ammonia. To investigate the degree of sp^2/sp^3 hybridization (here called the pyramidality) in the amine groups a parameter α is introduced. Based on the average of the CNH and HNH angles $\langle\theta\rangle$ in the amine groups, the pyramidality α is defined as:

$$\langle\theta\rangle = \alpha \cdot \theta_{sp^3} + (1-\alpha)\cdot\theta_{sp^2},\ \alpha = \frac{\langle\theta\rangle - \theta_{sp^2}}{\theta_{sp^3} - \theta_{sp^2}}$$

where $\theta_{sp^2} = 120^\circ$ (perfect plane) and $\theta_{sp^3} = 107^\circ$ (perfect trigonal pyramidal geometry). A pyramidality parameter of 1 is then equivalent to the amine group being fully sp^3 hybridized while 0 is fully sp^2 hybridized, as visualized in Figure 3.

To investigate the discrepancy from the apparent D_{3h} symmetry of the melamine molecule, theoretical gas phase geometry optimizations were conducted. Two geometry optimizations were performed, one starting from the C_1 experimental geometry obtained from SCXRD, and the other from a symmetrized D_{3h} geometry. No further symmetry constraints were applied during the optimizations. Bond lengths and angles of the two optimized structures, as well as the experimental structure can be seen in Table 1. The symmetrized geometry reached an unstable D_{3h} structure through the optimization, as apparent from negative vibrational frequencies. This is likely due to the starting symmetry keeping the geometry in a false minimum. Optimizing the experimental geometry results in a stable structure where all bonds and angles between non-hydrogen elements obey the D_{3h} symmetry, but the hydrogen atoms in the amine groups are bent slightly out of the plane defined by the ring with a torsion angle of up to 13.6°, reducing the point group symmetry to C_1. Two of the amine groups have the hydrogen atoms bent the same way out of the molecular plane while the latter is opposite.

The symmetrized geometry has $\alpha = 0$, corresponding to sp^2 hybridized amine groups. The optimized experimental geometry has $\alpha = 0.12$ for all amine groups suggesting that slightly more sp^3-like character of the amine groups is favorable in the gas phase. The experimental geometry has two amine groups with α parameters of 0.07 and 0.05 corresponding to an almost fully sp^2 hybridized character for N(4) and N(5), while the third amine group, N(6), has an α parameter of 0.44 suggesting a significantly higher degree of sp^3 character in this group. Since it holds for both gas phase calculations that all three amine groups in the molecule have the same α parameter, the reduced symmetry in the experimental structure must arise from crystal effects, creating a favorable environment for the N(6) amine group to be in a state between sp^3 and sp^2 hybridization.

To determine the origin of the discrepancy between the amine groups in the experimental geometry, the electronic properties of melamine have been characterized by topological analysis. In Table 2 we show results from the topological analysis of the experimental ED (top row for each bond critical point (bcp)), as well as the theoretical multipole projected ED (middle row) and the wave function based ED (bottom row) for comparison. The agreement between the three results is

Table 1. Geometry of the melamine molecule from experiment, as well as theoretical geometry optimization computed at the B3LYP/6-311G(d,p) level starting from a theoretical gas-phase structure and the experimental crystalline structure with D_{3h} and C_1 point-group symmetry respectively. Properties for the experimental geometry are shown as ranges. Amine HNH angles and pyramidality for the experimental geometry are tabulated in the order N(4)/N(5)/N(6). The energy is in units of Hartree [H].

		Sym. opt.	Exp. opt.	Experimental
	Symmetry	D_{3h}	C_1	C_1
	Energy [H]	−446.623	−446.623	−446.621
	Comment	Neg. freq		Neg. freq
Bond length [Å]	CN_{ring}	1.341	1.341	1.338–1.352
	CN_{amine}	1.355	1.359	1.339–1.362
	NH	1.004	1.005	0.993–1.008
Angle [°]	NCN_{ring}	126.36	126.3	124.8–125.7
	CNC_{ring}	113.64	113.7	114.6–114.8
	NCN_{amine}	116.82	116.8	116.5–118.2
	CNH	119.28	118	113.4–119.9
	HNH	121.44	119.5	118.4/121.4/114.1
Torsion [°]	$CNCN_{ring}$	0	<1	<3.6
	$CNCN_{amine}$	0	1.3–2.0	1.5–4.2
	NCNH	0	11.1–13.6	3.8–25.3
Pyramidality	α	0	0.12	0.07/0.05/0.44

Table 2. Results from the topological analysis of the electron density showing intramolecular C–N(amine) bcps. The first row for each bcp is from the experimental multipole model, the second is from the periodic theoretical multipole model (based on CRYSTAL17 structure factors) and the third is from the theoretical periodic wave function based density (calculated with TOPOND). d1 and d2 are the distances from the first mentioned atom, i, to the bcp and from the bcp to the latter atom, j, respectively. R_{ij} is the distance from atom i to j along the bond path. ρ is the density, $\nabla^2\rho$ the Laplacian and ε the bond ellipticity. G, V and H are the the kinetic, potential and total energies, respectivly given in Hartree/Å^3 [H/Å^3]. The remaining intramolecular bcps and further information can be found in Table S9.

Bond	*D*1 [Å]	*D*2 [Å]	R_{ij} [Å]	ρ[e Å^{-3}]	$\nabla^2\rho$ [e Å^{-5}]	ε	*G* [H Å^{-3}]	*V* [H Å^{-3}]	*V*/*G*	*H* [H Å^{-3}]
C(1)–N(4)	0.513	0.826	1.339	2.414	−33.842	0.27	1.913	−6.196	3.238	−4.282
	0.583	0.756	1.339	2.302	−22.286	0.23	2.187	−5.934	2.713	−3.747
	0.521	0.818	1.339	2.281	−25.906	0.18	1.969	−5.751	2.921	−3.782
C(2)–N(5)	0.528	0.812	1.340	2.343	−31.885	0.24	1.835	−5.902	3.216	−4.067
	0.582	0.758	1.340	2.298	−21.914	0.23	2.195	−5.924	2.699	−3.729
	0.521	0.820	1.341	2.267	−25.834	0.18	1.941	−5.690	2.932	−3.749
C(3)–N(6)	0.544	0.819	1.363	2.237	−28.410	0.19	1.750	−5.490	3.136	−3.739
	0.594	0.768	1.362	2.198	−19.833	0.19	2.062	−5.512	2.673	−3.450
	0.545	0.818	1.362	2.193	−24.051	0.14	1.854	−5.392	2.908	−3.538

excellent. The larger α parameter of 0.44 for the N(6) amine group is well in accordance with the lower ED and ellipticity in the C(3)–N(6) bcp, seen in Table 2 and Figure 4, as well as a longer bond length (1.36 Å) compared to the two other C–N(amine) bonds (1.35 Å). Analysis of the Laplacian $\nabla^2\rho$ around the amine groups shows that for both the experimental geometry in the crystal and optimized experimental geometry in the gas phase, all amine nitrogen atoms exhibit one (3,+3) $\nabla^2\rho$ critical point, corresponding to lone pair density. The value of the $\nabla^2\rho$ in the lone pair critical points of the experimental geometry in the crystal, is significantly lower, $\nabla^2\rho = -59.3$ e Å^{-5}, for N(6) than the two others in the crystal geometry, with Laplacian values of −51.6 and −50.7 e Å^{-5} for N(4) and N(5), respectively. Thus, there is a larger electron concentration in the N(6) lone pair compared with the two others. In the gas phase optimized geometry where all amine groups are equivalent, the value of $\nabla^2\rho$ in the lone pairs was found to be just slightly higher (lower electron concentration) than for N(4) and N(5) in the experimental geometry, with a value of −48.1 e Å^{-5}. Meanwhile the symmetrized optimized geometry in the gas phase shows two (3,+3) $\nabla^2\rho$ critical points in the vicinity of the amine nitrogen atoms, just above and below the molecular plane, with an even higher $\nabla^2\rho$ value of −41.3 e Å^{-5}, supporting the previous conclusions that the amine groups are sp^2-hybridized in this geometry. These parameters all point towards a weaker C–N(amine) bond with less double bond character, and thus more sp^3 character for C(3)–N(6) in the crystal. For melamine to condense to g-CN it requires ammonia to evaporate from the structure. The weaker C–N bond and the fact that the geometry of the N(6) amine group resembles that of ammonia to a larger extent than the other amine groups, may suggest that this group plays a role in the condensation process.

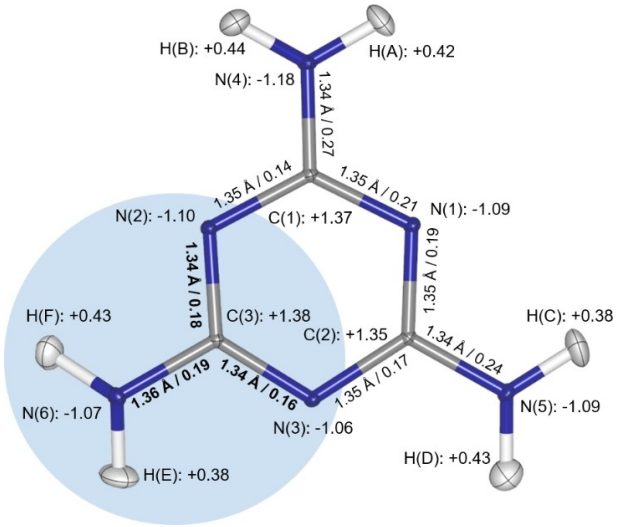

Figure 4. Visualization of results from the topological analysis of the experimental electron density. All values can be found in Tables S8 and S9 in the Supporting Information. Bader charges of each atom in units of e are written after the atom name (as "atom(number): Bader charge", for example, C(1) has a Bader charge of +1.37 e). Bond length and ellipticity are written next to the bond (as "bond length/−ellipticity", for example, the bond between C(1) and N(1) has a bond length of 1.3470 Å and an ellipticity of 0.21). The N(6) amine group and neighboring bonds are highlighted by a blue circle for emphasis.

The effect of the pyramidal amine groups can be visualized though the electrostatic potential (esp) map, where the electrostatic potential is mapped onto the ED at an isovalue of 0.0004 a.u. as seen in Figure 5. The esp of the experimental geometry is shown both as obtained from a theoretical gas phase calculation of the ED (denoted "Exp. Geometry (gas phase)") and from the experimental ED of the crystal (denoted "Exp. Geometry (crystal)"). The most negative potential value is at the nitrogen atoms in the ring. The major difference between the optimized geometries (top row in Figure 5) and the experimental geometry (bottom left in Figure 5) is observed when comparing the esp at the amine-nitrogen atoms to the ring-nitrogen atoms. For the experimental geometry, N(6) exhibits a very strong negative esp, similar to that of the ring-nitrogen atoms. Meanwhile the theoretical gas phase geometries show significantly less negative potentials at the amine-nitrogen atoms compared to the ring-nitrogen atoms. The esp in the crystal (bottom right in Figure 5) is remarkably different from the theoretically obtained esps. Not only is the shape of the isosurface different due to a different density landscape in the solid state, but the mapped esp also shows, that a remarkably strong negative potential covers the ring, in

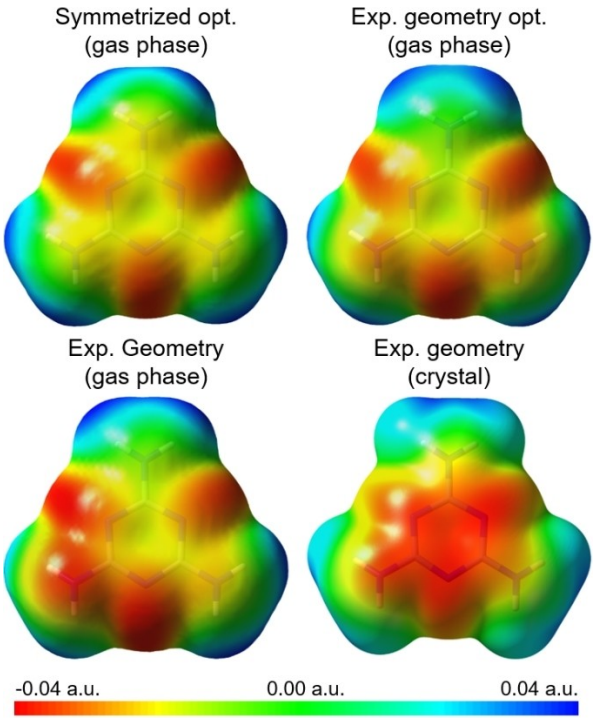

Figure 5. Electrostatic potential mapped at the 0.0004 a.u. electron density isovalue. The symmetrized opt.-, experimental opt.- and experimental geometry esps are obtained from the theoretical densities computed at the B3LYP/6-311G(d,p) level, while the crystal esp is obtained from the experimental electron density in the crystal. Molecules are oriented as in Figure 2.

contrast to the theoretical esps where the center of the ring is more or less neutral. Another feature of the crystal esp is observed at the hydrogen atoms, where the potential is slightly lower in the bond direction, than perpendicular to it, as evidence of hydrogen bonding. This is in line with results obtained from the energy framework calculations and topological analysis (see below), and clearly shows that the molecular geometry is influenced and altered by the intermolecular interactions in the crystal structure.

Energy frameworks

Energy framework calculations show that each molecule has four very strong electrostatic interactions of which two are symmetry equivalent with the energies −53.9, −58.3 and −70.5 kJ mol^{-1}. These interactions are between molecules at (*x*, *y*, *z*) coordinates and the molecules with the symmetry generated positions vi, vii/viii and ix, respectively, the symmetry codes are described in Table 3. Three of the interactions are in the layer (vii, viii and ix), while the fourth is between layers (vi), as seen in Figure 6. Dispersion interactions are dominant for molecular pairs at (*x*, *y*, *z*) and i, and (*x*, *y*, *z*) and ii/iii. The dispersion energies are close to or stronger than −20 kJ mol^{-1}, but significantly weaker than the electrostatic interactions, which is typical for strongly hydrogen bonded structures. The energy frameworks can be seen in Figure 6, with Figure 6a and b showing the strong interactions between the layers, and Figure 6c and d showing a single layer including weaker features as well. The strongest dispersion interactions are seen between layers, while coulomb interactions are strong both within and between the layers. Two weaker coulomb interactions are seen within the layer in addition to three of the four strongest coulomb interactions.

Several hydrogen atoms are bent significantly out of the layers, as can be seen in Figure 6a and b, a feature most pronounced in the case of the before mentioned N(6) amine group, where both hydrogen atoms are directed towards hydrogen bond acceptors in the adjacent layer. Hirshfeld Surface (HS) analysis[20] shows that in addition to the hydrogen bonding H···N contacts covering 43.1% of the surface, 8.1% arise from H···C contacts and 38.0% from H···H contacts. Due to the nature of the HS, describing close contacts, and not physical interactions, and the fact that no bcps are observed between such pairs of atoms (see below), further characterization of the H···C and H···H contacts has not been attempted. The HS and corresponding fingerprint plots of melamine can be seen in Figures S3 and S4.

Table 3. Energies of the energy frameworks in kJ/mol. The table shows the distance, R, between molecular center of masses and energy between a molecule at position (x, y, z) (asymmetric unit) to the symmetry generated molecules in the near vicinity, with symmetry codes as stated in the table. E_{ele} and E_{rep} are the classical electrostatic interaction energy and the exchange-repulsion energy, respectively. E_{pol} is the polarization energy and E_{dis} is the Grimme dispersion energy term. The total energy E_{tot} is given as a scaled sum of the contributions. Symmetry codes relate to the symmetry operation and translation in fractional coordinates: i) (1−x,1−y,1−z), ii) (x−$^1/_2$,$^3/_2$−y,z−$^1/_2$), iii) ($^1/_2$+x,$^3/_2$−y,$^1/_2$+z), iv) ($^3/_2$−x,y−$^1/_2$,$^1/_2$−z), v) ($^3/_2$−x,$^1/_2$+y,$^1/_2$−z), vi) (1−x,2−y,1−z), vii) ($^1/_2$−x,y−$^1/_2$,$^1/_2$−z), viii) ($^1/_2$−x,$^1/_2$+y,$^1/_2$−z), ix) (2−x,1−y,1−z), x) (x,1+y,z), xi) (x,y−1,z) and xii) (2−x,2−y,1−z).

Symmetry code	*R* [Å]	E_{ele}	E_{pol}	E_{dis}	E_{rep}	E_{tot}
i	3.86	0.9	−2.0	−27.5	10.9	−17.8
ii, iii	5.40	−8.7	−2.3	−18.9	16.5	−17.3
iv, v	5.48	0.1	−1.7	−15.1	8.1	−9.3
vi	5.95	−53.9	−12.9	−20.1	70.7	−40.3
vii, viii	6.09	−58.3	−13.9	−18.5	66.3	−47.1
ix	6.14	−70.5	−17.7	−19.4	87.0	−50.8
x, xi	7.46	−8.0	−1.3	−7.1	7.3	−11.1
xii	7.63	−10.5	−1.3	−8.0	7.6	−14.3

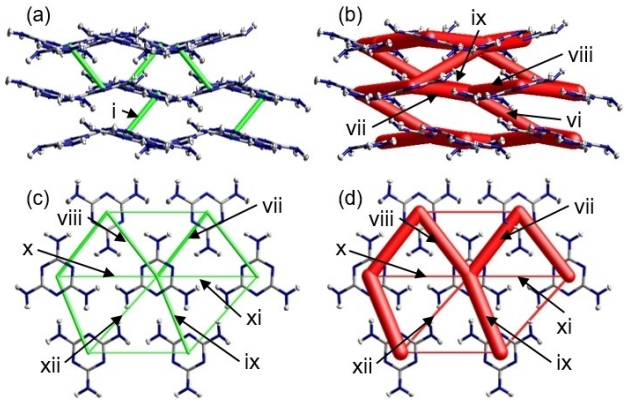

Figure 6. Energy frameworks computed at the B3LYP/6-31G(d,p) level. Dispersion energy (green) and coulomb energy (red). (a) and (b) are visualized parallel to the layers, the tube size corresponds to the strength of the interaction, and interactions weaker than -20 kJ mol^{-1} are excluded. (c) and (d) show the interactions inside one layer, visualized perpendicular to the layer. Again the tube size corresponds to the strength of the interaction, but no energy cut-off was applied in these figures. Symmetry codes can be seen in Table 3.

Topological analysis

Three different types of intermolecular interactions, C···C, N···N and N···H, are observed by topological analysis of the experimental ED and analyzed in accordance with Gatti.[21] Again experimental results are compared with similar analysis of theoretical densities from periodic calculations with excellent agreement, except the weaker C···C bcp, which is only found for the experimental density and not the theoretical densities. Table S10 shows properties of all unique intermolecular bcps from the molecule in the asymmetric unit to the symmetry related neighbors. The most relevant bcps will be discussed in detail later, but here we shortly mention the others for the sake of completeness. Firstly, a C···C π-interaction, C(1)···C(2)^{i}, with a bond path distance of 3.5 Å. Secondly, a weak N···N interaction between two amine nitrogen atoms, N(6)···N(4)^{iii}, with a bond length of 3.2 Å. The properties at these two bcps suggest that the interactions can be classified as weak closed-shell van der Waals interactions, but with a slightly covalent character. Both bond paths are shown in Figure 7. Dispersion interactions found by energy framework calculations are strongest for molecules at exactly the positions where the C···C and N···N bcps are found. Both interactions are between layers in the structure and are found by nci analysis to be of intermediate strength, as seen in Figure 10, below.

Four rather short hydrogen bonds are found between hydrogen atoms and ring nitrogen atoms, N(1)···H(B)^{vii}, N(2)···H-(A)^{viii}, N(2)···H(F)^{vi} and N(3)···H(D)^{ix}, with acceptor···H bond lengths close to 2.0 Å and acceptor···donor distances around 3.0 Å. All hydrogen bonds can be seen in Figure 8. Properties at the bcps and nci analysis classify the hydrogen bonds as strongly stabilizing, a conclusion which is supported by a strong coulomb interaction in the energy frameworks.

Two weaker hydrogen bonds, N(1)···H(E)^{ii} and N(6)···H(C)^{x}, are found in addition to the four strong bonds. N(6) is the only amine nitrogen which acts as a hydrogen bond acceptor, the bond path can be seen in Figure 9a. The N(6)···H(C)^{x} bond length is 2.59 Å and has a donor-H-acceptor, N(5)^{x}–H(C)^{x}···N(6), angle of 122.9°, suggesting a weaker interaction with only scarce directionality. The Laplacian map in Figure 9b visualized in a plane including the N(6)–H(C)^{x} hydrogen bond, shows clear ED concentration on N(6) in the direction of H(C)^{x}. This supports the hypothesis that favorable intermolecular interactions are the cause of the higher pyramidality in the N(6) amine group. The plot of the Laplacian value along the line between N(6) and H(C)^{x} in Figure 9c shows the standard mechanism of a well-defined hydrogen bond going from a $\nabla^2\rho$ (3, -3) critical point on the hydrogen atom to a $\nabla^2\rho$ (3, $+3$) critical point on the acceptor, in this case N(6).[22–23] The bond path between N(6) and H(C)^{x} is fairly straight with only very little deviation from the direct path. Therefore, the properties shown in Figure 9c are regarded as good estimates of the properties along the bond path.

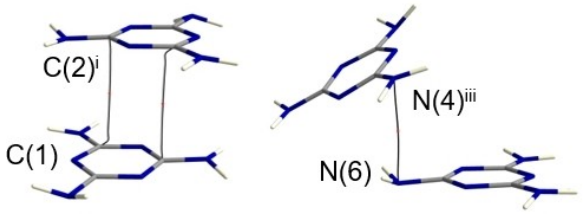

Figure 7. π-interactions confirmed by C(1)···C(2)^{i} bond critical points. Bond critical point between N(6) and N(4)^{iii}. Superscripted numbers indicate symmetry codes, which can be seen in Table 3.

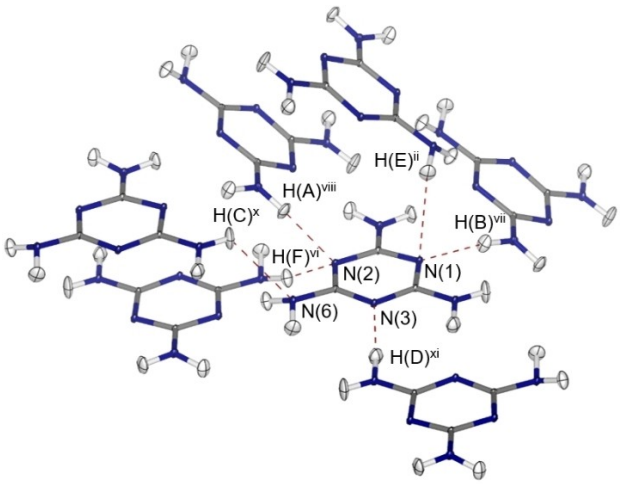

Figure 8. Hydrogen bonds visualized by dashed lines between atoms with bond critical points. Superscripted numbers indicate symmetry codes, which can be seen in Table 3.

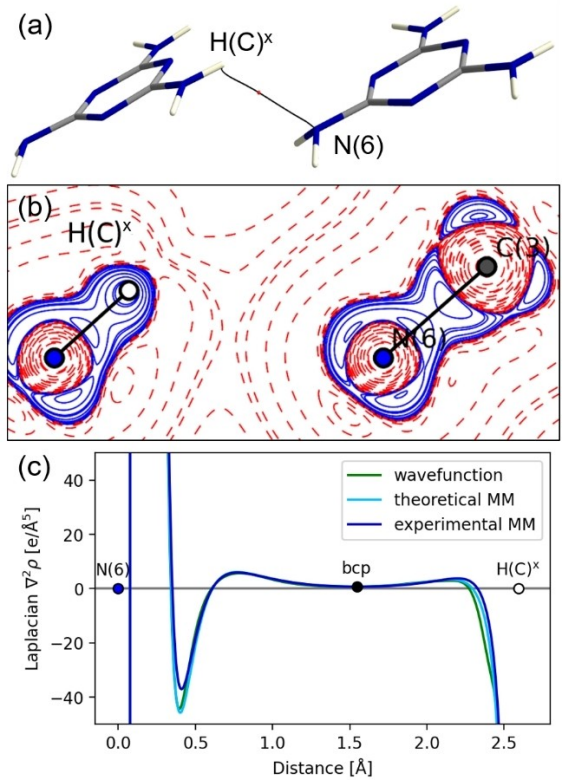

Figure 9. Bond path of the N(6)···H(C)^{x} hydrogen bond, the 2D Laplacian map in the plane defined by H(C)^{x}, N(6) and C(3) and a graph showing the value of the Laplacian along a line between N(6) and H(C)^{x}. Values are shown for the experimental electron density, and the periodic theoretical calculations (both from multipole projection and from wavefunction). Superscripted numbers indicate symmetry codes, which can be seen in Table 3. The Laplacian map is shown with logarithmic contour levels and a color scheme where red is positive, and blue is negative.

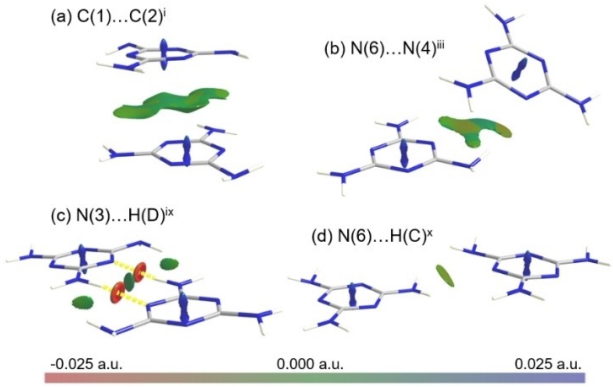

Figure 10. Noncovalent interaction maps between pairs of molecules. The sign of the Laplacian is mapped onto the 0.6 a.u. nci isosurface. The color scale ranges from red over green to blue indicating strongly stabilizing, intermediate and destabilizing interactions, respectively. (a), (b), and (d) Interactions of intermediate strength between C(1)···C(2)^{i}, N(6)···N(4)^{iii} and the weaker N(6)···H(C)^{x} hydrogen bond. (c) Strong hydrogen bonds between N(3)···H(D)^{ix} and the reverse H(D)···N(3)^{ix}. Superscripted numbers indicate symmetry codes, which can be seen in Table 3.

Noncovalent interactions analysis

Strong hydrogen bonds give a very characteristic donut shaped feature of the nci isosurface, as seen in Figure 10c. Even though an nci isosurface is found between N(6) and H(C)^{x} and the Laplacian properties on the path between N(6) and H(C)^{x} shows the same features as other hydrogen bonds, the nci isosurface does not show the characteristic shape of a hydrogen bond (Figure 10d), but instead resembles that of the C···C or N···N interactions (Figure 10a and b), confirming the weaker nature.

Condensation mechanism

Analysis of the molecular geometry shows that the N(6) amine group has a different hybridization than predicted by gas phase calculations, summarized in the α value of 0.44 signifying a high pyramidality. We suggest that this discrepancy is due to the fact that N(6) is the only amine nitrogen accepting a hydrogen bond. All ring nitrogen atoms act as hydrogen bond acceptors, but N(4) and N(5) only act as donors (of the N(2)···H(A)^{viii}-N(4)^{viii}, N(1)···H(B)^{vii}-N(4)^{vii} and N(6)···H(C)^{x}-N(5)^{x}, N-(3)···H(D)^{ix}-N(5)^{ix} hydrogen bonds, respectively). N(6) also acts as a donor like the other amine nitrogen atoms (for the N(1)···H-(E)^{ii}—N(6)^{ii} and N(2)···H(F)^{vi}—N(6)^{vi} hydrogen bonds), but is unique in the sense that it also acts as an acceptor. Other N···H pairs may be bonded stronger, but the unique situation of two amine groups interacting, required for the condensation to take place, is only fulfilled for the N(6)···H(C)^{x} hydrogen bond. We hypothesize that during the condensation process from melamine to g-CN, the structure may rearrange such that the N(6) amine group attracts H(C)^{x}, and evaporates from the structure as ammonia. The N(6)···H(C)^{x} hydrogen bond lies within layers, suggesting a condensation within each layer, supported by the similar interlayer distances in melamine and g-CN. Elimination of N(6) as ammonia and condensation through N(5) has several possible outcomes. If nothing else in the structure changes, a 1D polymer would be formed, but this is highly unlikely, due to the relatively long intermolecular distance (compared to a C–N bond) requiring some rearrangement to take place. Furthermore, in-situ PXRD studies have shown that the pathway to g-CN has melam as an intermediate product, so it is more likely that isolated melam molecules are formed in the first step, and then condenses further into g-CN.[8]

Conclusions

The molecular geometry of melamine in the solid state was compared to theoretical gas-phase geometry optimizations, and it was found that the intermolecular interactions in the crystal have a vital impact on the molecular geometry. Two of the three amine groups in melamine were found to exhibit properties close to sp^{2} geometry where the amine group is almost flat and in plane with the ring, presumably contributing ED from the nitrogen lone pair to the *s*-triazine aromatic system. The donation of ED to the π-system was confirmed by the higher ellipticity and ED at the intramolecular C–N(amine) bcps

for these two amine groups compared to the third amine group. The N(6) amine group was significantly more pyramidal in shape, and it was found that this deviation from the sp^2 geometry coincides with a favorable hydrogen bond. Both hydrogen bonds where N(6) acts as a donor have acceptors in the adjacent layer, while the other two amine groups only participate in intralayer hydrogen bonding. Furthermore, N(6) is the acceptor of a weaker intralayer hydrogen bond as the only amine nitrogen atom acting as a hydrogen-bond acceptor.

Intermolecular interactions were investigated through topological analysis of the experimentally determined ED, as well as the theoretical multipole-projected ED and the wave-function-based ED from periodic calculations. All results were supported by theoretical energy framework calculations on the experimental geometry. Hydrogen bonding and π-interactions dominate the intermolecular interactions in melamine in the crystalline form. Hydrogen bonding dominates within layers, while both hydrogen bonds and dispersion interactions between carbon pairs and nitrogen pairs were found between layers.

The layered structure of melamine molecules in the crystal with similar interlayer distance, as in g-CN, cements the resemblance between the precursor and the final material. We hypothesize that melamine condenses to g-CN within the layers. Analysis of both the molecular geometry and intermolecular interactions suggests that one amine group is unique and is proposed to play a role in the condensation process. The results presented in this paper emphasize the close relation between the melamine structure and CN materials.

Experimental Section

Synthesis: The synthesis used in this study is the same as in a study by Larsen et al.,[8] but with an adjusted heating scheme. Approximately 10 g of ammonium thiocyanate was loaded into an open porcelain crucible, which was placed in a quartz tube fitted into a vertical tube furnace and heated at 300 °C for 1.5 h. The product was washed and approx. 1 g was placed in a 75 cm long quartz ampule. The ampule was placed in a tube furnace with the powder-end in the center of the oven, while the other end reached outside. The temperature was then ramped up from room temperature with 1 °C min^{-1} to 400 °C, where the temperature was kept stable for 10 h. The produced crystals were rod-shaped transparent single crystals with distinct facets with a size range from a few micrometers up to one millimeter. SCXRD showed the crystals to be melamine.

Crystallographic details: A block shaped melamine single crystal with a diameter of ca. 140 μm was used for measurements at the BL02B1 beamline at the SPring-8 synchrotron in Japan. An X-ray energy of 50 keV, corresponding to a wavelength of 0.2480 Å, was used, and the crystal was cooled to 25 K using a liquid He jet stream. The beamline is equipped with a quarter χ goniometer and a Pilatus3 x 1 M CdTe detector. For a complete set of data, six 180° ω scans were collected at χ values of 0°, 20° and 40° for 2θ values of 0° and −20°, respectively. No attenuation was used, enabling a short exposure time of 0.14 s/frame and a scan width of 0.5 °/frame. In total 10800 frames were collected.

Data obtained from SPring8 was converted to Bruker format using the Pilatus3 frame conversion software developed by Krause.[24] Data reduction was performed in the Apex3 GUI for the program SAINT[25] with the recurrence background setting. SADABS[26] was used for scaling and absorption correction of the integrated data, while the SORTAV[27] program was used for the rejection of outliers, merging of the equivalent reflections and to obtain estimates of their uncertainties.

Melamine crystallizes in the $P2_1/n$ monoclinic space group, with lattice parameters of 7.2355(2) Å, 7.4554(2) Å and 10.0871(3) Å, and a β angle of 107.9240(13)°. All atoms are placed on general positions. The unit cell contains four formula units, resulting in a density of 1.618 g cm^{-3}. A summary of the crystallographic details can be seen in Table 4 and further comments can be found in the Supporting Information. Deposition Number 2172057 contains the supplementary crystallographic data for this paper. These data are provided free of charge by the joint Cambridge Crystallographic Data Centre and Fachinformationszentrum Karlsruhe Access Structures service.

Structure solution, Hirshfeld atom refinement and multipole modeling

The structure was solved using ShelXT[28] and the initial geometry was refined with an independent atom model (IAM) in ShelXL[28] using the Olex2[29] GUI. Estimates of the hydrogen positions and anisotropic vibrational parameters were obtained from Hirshfeld Atom Refinement (HAR)[30] on the experimental geometry. HAR was performed in Olex2 using the tool NoSpherA2.[31] Tonto was chosen with the basis set def2-SVP, the method B3LYP, a charge of zero and with the multiplicity set to one. A cluster with the radius 8 Å was defined for the calculation, and convergence was achieved.

An aspherical multipole ED model was refined against the merged reflections using the Hansen-Coppens multipolar formalism[32] in the XD2016[33] program. The initial geometry and thermal parameters were obtained from the HAR refinement. The Su, Coppens, Macchi radial function databank was used.[34–35] The hydrogen Atomic Displacement Parameters (ADPs) and bond lengths were

Table 4. Crystallographic and experimental information of the synchrotron X-ray diffraction experiment. *Number of unique reflections measured more than three times.

Parameter	Spring8
Formula	$C_3N_6H_6$
Formula weight [g mol^{-1}]	126.12
Crystal diameter [μm]	~140
Wavelength [Å]	0.248
Temperature [K]	25
Max sin θ/λ [$Å^{-1}$]	1.45
Crystal system	monoclinic
Space group	$P2_1/n$
a [Å]	7.2355(2)
b [Å]	7.4554(2)
c [Å]	10.0871(3)
$\alpha=\gamma$ [°]	90
β [°]	107.9240(13)
Volume [$Å^3$]	517.728(35)
Z	4
F(000)	264
ρ [g cm^{-3}]	1.618
μ [mm^{-1}]	0.033
Exposure time [s/frame]	0.14
R_{int} [%]	3.97
Mean I/σ	45.0
$N_{measured}$	164296
N_{unique}*	13231
Completeness [%]	100.0
Average redundancy	12.35

constrained to the values obtained from HAR. Atoms in chemically similar environments were given the same contraction/expansion parameters (κ parameters), two for the nitrogen atoms (ring, amine), one for carbon and one for hydrogen. For each set of atoms, the spherical κ value and one common κ' value for all multipoles were refined. For the initial refinements, all κ values, for nitrogen and carbon were set to unity, while hydrogen κ parameters were set to 1.15 and 1.4 for spherical κ and κ' respectively.[36] In the final model, κ and κ' parameters were refined without restrictions for all atoms.

Refinement included atomic positions, anisotropic atomic displacement parameters, monopoles, κ parameters, dipoles, quadrupoles, octupoles and hexadecapoles for all non-H atoms, for the hydrogen atoms only the bond-directed multipoles up to and including the quadrupolar level were refined. Tests performed to check the adequacy of the model, showed that neither anharmonic vibrational parameters on carbon and nitrogen, nor octupoles or hexadecapoles on hydrogen were significant within three standard deviations. Approximately half of the parameters describing the hexadecapoles on the p-block elements were significant within three standard deviations. Overfitting was tested according to the procedure of Krause et al.,[37] but no problems with overfitting were encountered. All values from the refinement can be found in Tables S1–S7.

The quality of the model was evaluated using a variety of tools summarized in Table 5. Comparing the observed and calculated structure factors squared in a binned plot (the F_{obs}^2/F_{calc}^2-plot) against $\sin\theta/\lambda$ gives an estimate of the intensity dependent errors. From the F_{obs}^2/F_{calc}^2-plot in Figure S1, a very high agreement between calculated and observed intensities can be seen. The blue horizontal line shows the ideal $y=1$ line, expected for full agreement. Binning the data should cancel out random errors. The largest deviation between observed and calculated structure factors squared is seen at low resolution where only few reflections are included in each bin, making the data points more susceptible to errors. The high agreement between calculated and observed intensities is also evident from the R-factor of 1.65 % based on F^2, which was obtained for refinements against data with a maximum $\sin\theta/\lambda$ of 1.45 Å^{-1}. The residual density map in Figure 11 (left) is practically featureless, meaning that the full ED is included in the multipole model. Residual density analysis gives the very narrow fractal dimension plots in Figure S2 with low max and min residuals of 0.20 and −0.14 e Å^{-3}, respectively.[38] The fractal dimension plot has a shape close to the desired parabolic shape, obtained for models with only stochastic errors, and a very narrow shape, obtained for models with only small errors. The shoulder at positive residuals indicates some kind of systematic error, but due to the low gross residual stating that only 0.012 e Å^{-3} were not described by the model, this was not investigated further. The Hirshfeld rigid bond test[39] showed successful deconvolution of thermal and electronic effects, as difference mean square amplitude for all bonding atom pairs are below the 10x10^{-4} Å^2 criterion for acceptable movement. The largest correlation coefficient of 0.82 is observed for monopoles on the amine nitrogen atoms, which is to be expected since this group of atoms has the same κ parameter, and the κ and monopole parameters are correlated in the Hansen-Coppens multipolar formalism.[32] Generally, from the shown parameters and plots it can be concluded that the model presented here is of remarkably high quality. The deformation density map in Figure 11 (middle) was found by subtracting the IAM model from the multipolar model. As expected, excess ED compared to the IAM model is seen in all bonding regions and as lone pairs on the nitrogen atoms in the ring. The valence charge on the hydrogen atoms is clearly displaced towards the bonding nitrogen, leaving a deficient area on the opposite site of the hydrogen atom. From the Laplacian map at the right in Figure 11, a significant overlap of valence charge in the amine groups can be observed, signifying a shared valence.[40] A slight elongation in the electron concentration in the direction of the hydrogen bond can be seen for some hydrogen atoms (e.g., H(A), H(C) and perhaps even more substantial on the hydrogen at a neighboring molecule with no label in the top left corner of the Laplacian map figure).

Theoretical structure factors with the same indices as the observed reflections were computed based on the experimental periodic

Table 5. Information for quality control of the multipolar model.

Parameter	SPring8
Max $\sin\theta/\lambda$ [Å^{-1}]	1.45
$R(F)$ [%]	1.36
$R(F^2)$ [%]	1.64
GOF	1.0873
*N*ref/*N*v	33.21
# reflections	11027
Gross residual [e Å^{-3}]	0.012
Min residual [e Å^{-3}]	−0.14
Max residual [e Å^{-3}]	0.20
Max correlation coefficient	0.82: M(1) on N(4), N(5) and N(6)
DMSA (Hirshfeld rigid bondtest)	All p-block atoms below 10×10^{-4} Å^2.

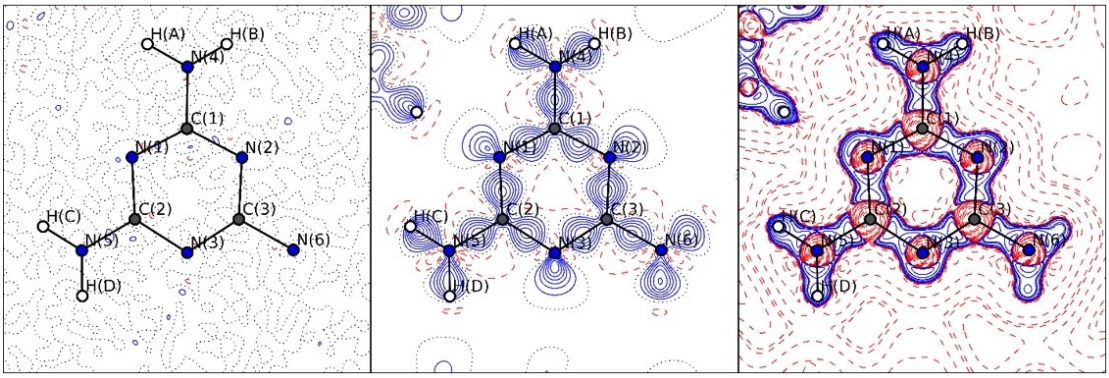

Figure 11. Residual density map and deformation density map, with contour lines at 0.1 e Å^{-}Å^3. Positive (solid blue), zero (dotted black), and negative (solid red) contours are shown, along with laplacian map, with logarithmic contour levels and the inverse color scheme ((this bit wasn't a sentence)). Both deformation density and laplacian maps are calculated in a 2×2×2 cell.

structure in CRYSTAL17 with the pob-TZVP-rev2 basis set.[41–43] A theoretical multipole-projected ED distribution was derived from the theoretical structure factors in XD2016, with the same strategy as for the experimental multipole model, but with a separate κ and monopole for the core electrons. A reasonable model was obtained with $R(F) = 0.5$, GOF = 3.630 and min/max residuals of -0.24 and $+0.39$ e Å^{-3}. From the same geometry a wave function based density was derived and used for further analysis in TOPOND.[22,44] Topological analysis was carried out in the framework of Bader's Quantum theory of atoms in molecules, see Table 2 and the Supporting Information.[45]

The main part of the discussion in this study is based on the position of the hydrogen atoms in the asymetric unit. The hydrogen atom position is challenging to determine from X-ray diffraction experiments due to the so called aspherical shift related to the displacement of the entire ED on hydrogen into the chemical bond.[46] The high data quality used in this study makes it possible to determine the hydrogen atom position accurately. Figure S5 shows the residuals of the IAM model when no hydrogen atoms are present. Hydrogen atoms are visualized for clarity, and it is observed that the density is significantly distorted away from the plane of the triazine ring, towards the hydrogen bond acceptor. The bond lengths reported in this study are in excellent agreement with values obtained from neutron diffraction studies at room temperature by Varghese et al. and at 14 K by Cousson et al.[18,47] A direct comparison of the room temperature study to our experiment at 25 K will not be conducted, but since the bond lengths within the melamine molecule have been reported to change very little when exposed to extreme environments,[1] we believe that the resemblance still serves as a quality asurance. With temperatures as low as 14 and 25 K we expect no significant differences arising from thermal effects. The 14 K neutron study reports a unit cell volume of 517.26(14) Å^3, which is very close to the 517.728(35) Å^3 reported in this study. A comparison of the hydrogen bond lengths and ADPs from a freely refined IAM, the final HAR and the neutron experiment can be seen in Table S11 and Figure S6. The average bond length difference between HAR and neutron data is 1%, whereas the IAM has an average deviation of 10% from the neutron values. The H–N–H angles for the N(4)/N(5)/N(6) amine groups of 119.6°/119.0°/113.9° found in the neutron study and the corresponding α parameters of 0.08/0.07/0.42 are comparable to those presented in Table 1. The HAR and neutron ADPs were compared using the UIJXN program,[48] giving a mean ratio, $\langle U_{ii}(X)/U_{ii}(N)\rangle$, and absolute mean deviation, $\langle \Delta U\rangle$, of 1.5(5) and 0.00174, respectivly, for the p-block elements, and 1.0(3) and 0.00786, respectivly, for the hydrogen atoms. These values are relatively high compared with high-quality X–N studies reported in the literature, suggesting that systematic errors are present in the two data sets. Judging from the very high quality ED refined from the X-ray data, the discrepancy is likely due to inferior neutron data quality.[48–50] The IAM p-block ADPs are in fairly good agreement with the two other models, but the hydrogen ADPs are significantly larger, and deviates unphysically much in magnitude. With a starting geometry obtained from HAR and the high quality of the multipolar model used, we are confident that the hydrogen atom parameters reported in this study are trustworthy.

Theoretical calculations

Gaussian: Gas phase self-consistent field (SCF) calculations and geometrical optimizations were performed in Gaussian16[51] using the density functional theory (DFT) method with a B3LYP functional and the 6-311G(d,p) basis set. Topological analysis of the gas phase optimized geometry densities was carried out in the program AIMAll.[52]

Crystal explorer: The CrystalExplorer program[53] was used for HS analysis[20] and to calculate energy frameworks from the experimental geometry using B3LYP/6-31G(d,p) functional and basis-set. This may seem like a crude density estimate, but several publications have shown it to be sufficient and perform favorably compared to benchmarking datasets of higher quality with respect to both computational time and calculated energies for energy framework calculations of small closed shell systems with light atoms.[54–55]

Acknowledgements

The work was supported by the Villum Foundation. This work was partly supported by the Japan Society for the Promotion of Science (JSPS) Grants-in-Aid for Scientific Research (KAKENHI) Grant Number JP19KK0132, JP20H4656, and JP2105235. The synchrotron experiments were performed at SPring-8 BL02B1 with the approval of the Japan Synchrotron Radiation Research Institute (JASRI) (Proposals no. 2018b0078, no. 2019a0159 and no 2021a1744).

Conflict of Interest

The authors declare no conflict of interest.

Data Availability Statement

The data that support the findings of this study are available from the corresponding author upon reasonable request.

Keywords: chemical bonding · electron density · graphitic carbon nitride · melamine · synchrotron X-ray diffraction

[1] H. Shelton, P. Dera, S. Tkachev, *Crystals* **2018**, *8*, 265.
[2] Y. Zhang, Q. Pan, G. Chai, M. Liang, G. Dong, Q. Zhang, J. Qiu, *Sci. Rep.* **2013**, *3*, 1943.
[3] K. Qi, S.-y. Liu, A. Zada, *J. Inst. Chem.* **2020**, *109*, 111–123.
[4] A. Thomas, A. Fischer, F. Goettmann, M. Antonietti, J.-O. Müller, R. Schlögl, J. M. Carlsson, *J. Mater. Chem.* **2008**, *18*, 4893–4908.
[5] T. Komatsu, *Macromol. Chem. Phys.* **2001**, *202*, 19–25.
[6] Z. J. Zhang, S. Fan, C. M. Lieber, *Appl. Phys. Lett.* **1995**, *66*, 3582–3584.
[7] J. Sehnert, K. Baerwinkel, J. Senker, *J. Phys. Chem. B* **2007**, *111*, 10671–10680.
[8] F. K. Larsen, A. Hasen Mamakhel, J. Overgaard, J.-E. Jorgensen, K. Kato, B. Brummerstedt Iversen, *Acta Crystallogr. Sect. B* **2019**, *75*, 621–633.
[9] S. Matsumoto, E. Q. Xie, F. Izumi, *Diamond Relat. Mater.* **1999**, *8*, 1175–1182.
[10] T. Komatsu, *J. Mater. Chem.* **2001**, *11*, 799–801.
[11] A. Azoulay, J. Barrio, M. Shalom, *Isr. J. Chem.* **2020**, *60*, 544–549.
[12] G. Algara-Siller, N. Severin, S. Y. Chong, T. Björkman, R. G. Palgrave, A. Laybourn, M. Antonietti, Y. Z. Khimyak, A. V. Krasheninnikov, J. P. Rabe, U. Kaiser, A. I. Cooper, A. Thomas, M. J. Bojdys, *Angew. Chem. Int. Ed.* **2014**, *53*, 7450–7455; *Angew. Chem.* **2014**, *126*, 7580–7585.
[13] J. Jiang, L. Ou-yang, L. Zhu, A. Zheng, J. Zou, X. Yi, H. Tang, *Carbon* **2014**, *80*, 213–221.
[14] X. Wang, S. Blechert, M. Antonietti, *ACS Catal.* **2012**, *2*, 1596–1606.
[15] E. Hughes, *J. Am. Chem. Soc.* **1941**, *63*, 1737–1752.
[16] P. Price, J. Varghese, E. Maslen, *Acta Crystallogr. Sect. A* **1978**, *34*, 203–216.
[17] D. T. Cromer, A. C. Larson, R. F. Stewart, *J. Chem. Phys.* **1976**, *65*, 336–349.

[18] J. Varghese, A. O'Connell, E. Maslen, *Acta Crystallogr. Sect. B* **1977**, *33*, 2102–2108.
[19] M. Gryl, S. Cenedese, K. Stadnicka, *J. Phys. Chem. C* **2015**, *119*, 590–598.
[20] M. A. Spackman, D. Jayatilaka, *CrystEngComm* **2009**, *11*, 19–32.
[21] C. Gatti, *Zeitschr. Krist. Cryst. Mater.* **2005**, *220*, 399–457.
[22] C. Gatti, V. R. Saunders, C. Roetti, *J. Chem. Phys.* **1994**, *101*, 10686–10696.
[23] C. Flensburg, S. Larsen, R. F. Stewart, *J. Phys. Chem.* **1995**, *99*, 10130–10141.
[24] L. Krause, https://github.com/LennardKrause/.
[25] Bruker, in *SAINT + Integration Engine Reference Version 8.38 A Bruker AXS Inc.*, **2012**.
[26] L. Krause, R. Herbst-Irmer, G. M. Sheldrick, D. Stalke, *J. Appl. Crystallogr.* **2015**, *48*, 3–10.
[27] R. Blessing, *J. Appl. Crystallogr.* **1997**, *30*, 421–426.
[28] G. Sheldrick, *Acta Crystallogr. Sect. A* **2008**, *64*, 112–122.
[29] O. V. Dolomanov, L. J. Bourhis, R. J. Gildea, J. A. K. Howard, H. Puschmann, *J. Appl. Crystallogr.* **2009**, *42*, 339–341.
[30] S. C. Capelli, H.-B. Burgi, B. Dittrich, S. Grabowsky, D. Jayatilaka, *IUCrJ* **2014**, *1*, 361–379.
[31] F. Kleemiss, O. V. Dolomanov, M. Bodensteiner, N. Peyerimhoff, L. Midgley, L. J. Bourhis, A. Genoni, L. A. Malaspina, D. Jayatilaka, J. L. Spencer, F. White, B. Grundkötter-Stock, S. Steinhauer, D. Lentz, H. Puschmann, S. Grabowsky, *Chem. Sci.* **2021**, *12*, 1675–1692.
[32] N. K. Hansen, P. Coppens, *Acta Crystallogr. Sect. A* **1978**, *34*, 909–921.
[33] P. M. A. Volkov, L. J. Farrugia, C. Gatti, P. R. Mallinson, T. Richter, T. Koritsanszky, Program XD2016, **2016**.
[34] Z. Su, P. Coppens, *Acta Crystallogr. Sect. A* **1998**, *54*, 646–652.
[35] P. Macchi, P. Coppens, *Acta Crystallogr. Sect. A* **2001**, *57*, 656–662.
[36] A. Volkov, Y. A. Abramov, P. Coppens, *Acta Crystallogr. Sect. A* **2001**, *57*, 272–282.
[37] L. Krause, B. Niepotter, C. J. Schurmann, D. Stalke, R. Herbst-Irmer, *IUCrJ* **2017**, *4*, 420–430.
[38] K. Meindl, J. Henn, *Acta Crystallogr. Sect. A* **2008**, *64*, 404–418.
[39] F. Hirshfeld, *Acta Crystallogr. Sect. A* **1976**, *32*, 239–244.
[40] K. Tolborg, M. R. V. Jørgensen, M. Sist, A. Mamakhel, J. Overgaard, B. B. Iversen, *Chem. Eur. J.* **2019**, *25*, 6814–6822.
[41] R. Dovesi, A. Erba, R. Orlando, C. M. Zicovich-Wilson, B. Civalleri, L. Maschio, M. Rérat, S. Casassa, J. Baima, S. Salustro, B. Kirtman, *WIREs Comput. Mol. Sci.* **2018**, *8*, e1360.
[42] M. F. Peintinger, D. V. Oliveira, T. Bredow, *J. Comput. Chem.* **2013**, *34*, 451–459.
[43] D. Vilela Oliveira, J. Laun, M. F. Peintinger, T. Bredow, *J. Comput. Chem.* **2019**, *40*, 2364–2376.
[44] C. Gatti, S. Casassa, Program TOPOND, CNR-ISTM of Milano, Milano, **2013**.
[45] R. F. W. Bader, *Atoms in Molecules: A Quantum Theory*, Clarendon, Oxford, **1994**.
[46] P. Coppens, *X-ray Charge Densities and Chemical Bonding*, Oxford University Press, New York, **1997**.
[47] A. Cousson, B. Nicolai, F. Fillaux, *Acta Crystallogr. Sect. E* **2005**, *61*, o222-o224.
[48] R. Blessing, *Acta Crystallogr. Sect. B* **1995**, *51*, 816–823.
[49] B. B. Iversen, F. K. Larsen, B. N. Figgis, P. A. Reynolds, A. J. Schultz, *Acta Crystallogr. Sect. B* **1996**, *52*, 923–931.
[50] W. Morgenroth, J. Overgaard, H. F. Clausen, H. Svendsen, M. R. V. Jorgensen, F. K. Larsen, B. B. Iversen, *J. Appl. Crystallogr.* **2008**, *41*, 846–853.
[51] M. J. Frisch, G. W. Trucks, H. B. Schlegel, G. E. Scuseria, M. A. Robb, J. R. Cheeseman, G. Scalmani, V. Barone, G. A. Petersson, H. Nakatsuji, X. Li, M. Caricato, A. V. Marenich, J. Bloino, B. G. Janesko, R. Gomperts, B. Mennucci, H. P. Hratchian, J. V. Ortiz, A. F. Izmaylov, J. L. Sonnenberg, Williams, F. Ding, F. Lipparini, F. Egidi, J. Goings, B. Peng, A. Petrone, T. Henderson, D. Ranasinghe, V. G. Zakrzewski, J. Gao, N. Rega, G. Zheng, W. Liang, M. Hada, M. Ehara, K. Toyota, R. Fukuda, J. Hasegawa, M. Ishida, T. Nakajima, Y. Honda, O. Kitao, H. Nakai, T. Vreven, K. Throssell, J. A. Montgomery Jr., J. E. Peralta, F. Ogliaro, M. J. Bearpark, J. J. Heyd, E. N. Brothers, K. N. Kudin, V. N. Staroverov, T. A. Keith, R. Kobayashi, J. Normand, K. Raghavachari, A. P. Rendell, J. C. Burant, S. S. Iyengar, J. Tomasi, M. Cossi, J. M. Millam, M. Klene, C. Adamo, R. Cammi, J. W. Ochterski, R. L. Martin, K. Morokuma, O. Farkas, J. B. Foresman, D. J. Fox, *Gaussian16*, Wallingford, CT, **2016**.
[52] T. A. Keith, *TK Gristmill Software*, Overland Park KS, USA, **2019**.
[53] P. R. Spackman, M. J. Turner, J. J. McKinnon, S. K. Wolff, D. J. Grimwood, D. Jayatilaka, M. A. Spackman, *J. Appl. Crystallogr.* **2021**, *54*, 1006–1011.
[54] C. F. Mackenzie, P. R. Spackman, D. Jayatilaka, M. A. Spackman, *IUCrJ* **2017**, *4*, 575–587.
[55] M. J. Turner, S. Grabowsky, D. Jayatilaka, M. A. Spackman, *J. Phys. Chem. Lett.* **2014**, *5*, 4249–4255.

Manuscript received: April 26, 2022
Accepted manuscript online: June 27, 2022
Version of record online: August 3, 2022